Solution-processed asymmetry conjugated reticular oligomers for large-area panel photoelectrodes in photoelectrochemical devices

Yazhou Kang [a,1], Boying Zhang [b,1], Ying Zhao [a,1], Huimin Gao [a], Xiaoming Li [a], Ruijuan Zhang [c], Pengda Zhai [a], Haining Liu [a], Shanlin Qiao [a,d,*]

[a] *College of Chemistry and Pharmaceutical Engineering, Hebei University of Science and Technology, Shijiazhuang 050018, China*
[b] *Department of Chemical Engineering, Faculty of Engineering and the Built Environment, University of Johannesburg, Doornfontein 2028, South Africa*
[c] *Institute for Catalysis and Energy Solutions, University of South Africa, Florida 1709, South Africa*
[d] *Hebei Engineering Research Center of Organic Solid Photoelectric Materials for Electronic Information, Shijiazhuang 050018, China*

ARTICLE INFO

ABSTRACT

Covalent organic frameworks (COFs) show potential in photoelectrochemical (PEC) water reduction. Herein, we synthesize solution-processed benzoxazole-based conjugated reticular oligomers (BBO-CROs) in micelle nano-reactors, acting as an "electronic paint" for fabricating consecutive panel-type photoelectrodes for PEC water reduction. The small-molecule BBO-CRO$_{PDA}$, BBO-CRO$_{DHTA}$, and BBO-CRO$_{BPY}$ exhibit a narrower energy bandgap and prolong the fluorescence lifetimes of photoinduced charge carriers compared to bulk BBO-COFs. Colloidal COFs in PEC water reduction are illustrated through the creation of flexible full devices *via* spinning coating. The optimized photoelectrode CuI/BBO-CRO$_{BPY}$+P27/SnO$_2$/Pt result in ΔJ of 86.5 µA cm^{-2} at 0.4 V *vs.* RHE, which is 86.5 times higher than that of bulk BBO-COF$_{BPY}$. The CuI/BBO-CRO$_{BPY}$+P27/SnO$_2$/Pt photo-electrode with an area of 100 cm^2 displays an impressive ΔJ of 82.0 µA cm^{-2} with good durability. A flat photoelectrode surface and the generation of photogenerated charge carriers under light are observed using scanning electrochemical microscopy (SECM) as an *in-situ* technique. Density Functional Theory (DFT) calculation indicates that the asymmetry of the BBO unit prompts electrons to preferentially move in a defined direction upon light excitation in the small-molecular framework, thereby suppressing electron backflow. This work overcomes COF processability limitations in PEC water reduction and paves the way for using flexible devices.

1. Introduction

Hydrogen, esteemed for its high energy density, zero emissions, and renewability, stands as a pivotal strategy in the arsenal of solutions to combat climate change and address the looming energy crisis [1]. Electrochemical hydrogen evolution reaction (HER) emerges as a promising and efficient avenue to produce clean and sustainable hydrogen energy [2]. Despite extensive efforts directed towards advancing the HER, the persisting challenges of relatively limited efficiency and reliance on external power sources continue to impede the progression of hydrogen generation. In the realm of HER, beyond the conventional electrocatalytic hydrogen generation driven solely by electric energy, the photo-coupled electrocatalytic method offers a promising avenue for achieving heightened activity in this process

[3–6]. Light irradiation exerts a profound influence on the electronic characteristics of light-sensitive electrocatalysts, leading to substantial modifications in the catalytic processes and activity of the HER. There is a practical significance to develop a photo-coupled electrocatalysis energy complementary system to further explore hydrogen generation [7, 8]. Photoelectrochemical (PEC) cells for water reduction have been acknowledged as potential platforms facilitating the cost-effective production of fuel [9,10], for which the light-harvesting and hydrogen fuel generation are integrated at a direct semiconductor−liquid interface within these systems [11]. The effective integration of electric and solar energy is necessary for a photoelectrode in PEC water reduction. This integration requires simultaneous fulfillment of the following prerequisites: (i) The presence of efficacious catalytic active sites for water reduction, and (ii) the capacity for conductivity, efficient light

---

absorption, and photoelectron conversion.

Despite numerous of study into the utilization of traditional inorganic semiconductors for artificial photosynthetic PEC water reduction, these configurations have not achieved the performance benchmarks essential for cost-effective and scalable industrial feasibility [12]. Organic semiconductors (OSs) are garnering growing interest as viable photoactive materials in the PEC water splitting [13, 14] OSs are distinguished by their molecular structures, consisting of either polymer or small molecules with extended π-conjugated structure [15]. These OSs exhibit a range of advantageous characteristics including the capacity for fine-tuning energy band levels through molecular engineering, as well as exceptional light-harvesting characterisics steaming from their relatively high molar extinction coefficients [16]. However, amorphous organic semiconductors face significant challenges in achieving uniformity of catalytic sites and reducing resistance to mass transport and diffusion limitations. Assembling individual active sites into highly ordered crystalline structures represent an optimal strategy for addressing the challenges. Two-dimensional covalent organic frameworks (2D COFs) with directional structural designability emerge as highly promising photo/electro-catalytic platforms due to their unique attribute of atomically precise arrangement of organic functional groups along the walls of their one-dimensional (1D) open pore channels. This distinctive feature endows them with well-defined active sites and fast mass transport as well as gas diffusion channels [17–20]. The electronic configuration, energy bandgap, light-harvesting capacity, active centers, and pore metrics can be readily customized *via* a bottom-up synthesis approach utilizing various building blocks [21]. However, even though the extended π-conjugated structure and long-range order arrangement might inherently support the transference of charge carriers, the progress of optoelectronic devices have been hindered by the challenging processability of COFs, since they are commonly obtained in the form of insoluble solids. Nowadays the primary obstacle in advancing PEC water reduction through the utilization of COFs as photoactive layers lies in the absence of effective strategies for preparing consecutive and smooth thin COF films or thin-multilayer heterojunction films photoelectrodes, that enable the efficient capture of photogenerated charges within the COFs. Efforts have been made to utilize substrate orientation [22], electrophoretic deposition [23], and solvothermal synthesis [21] for the generation of crystalline COF films and photoelectrodes. The attainment of COF films that exhibit macroscopic-scale coverage, homogeneousness, and controllable thickness at the nanometer level remains an intricate and formidable undertaking. Hence, innovative materials systems and methodologies for film preparation along with corresponding strategies to counteract photogenerated carrier recombination are imperative. The utilization of semiconductor inks for solution-processed thin film fabrication has emerged as a leading technology in the field of optoelectronic semiconductor devices [24,25]. Therefore, investigating a steady COF solution emerges as a potential strategy to overcome the inherent challenges associated with processing COFs for PEC water reduction.

Drawing insights from this concept, our research endeavors have been concentrated on the synthesis of solution-processed COF nanocrystals considering their unique ability to be engineered at the molecular level. The primary aim behind this effort is to attain meticulous command over the optoelectronic properties and processability of COFs. This control will enable the cost-effective production of large-scale layer printing or inkjet printing techniques for the development of panel-type photoelectrodes. In pursuit of this objective, we have focused on designing an efficient photoactive/electroactive monomer. The benzoxazole moiety was chosen due to its ability to absorb photon energy and provide abundant π-electrons and heteroatoms, enabling it to absorb and convert light into excited electrons [26–30]. These excited state electrons drive water reduction to produce hydrogen at the semiconductor film/electrolyte interface. The intricate interplay between molecular geometry and photochemical behavior highlights the pivotal role of molecular asymmetry in shaping the optical and electronic properties of the benzoxazole group.

Herein, we synthesized an asymmetric 4,4',4'',4'''-(benzo[1,2-d:4,5-d′]bis(oxazole)−2,4,6,8-tetrayl)tetraaniline (BBO) building block. The electron-donating BBO, along with terephthalaldehyde (PDA), 2,5-dihydroxyterephthalaldehyde (DHTA), and [2,2′-bipyridine]−5,5′-dicarbaldehyde (BPY), was integrated into the catanionic micellar size-confined nanoreactor to construct novel sub-5 nm solution-processed Donor−Acceptor (D−A) semiconductor nanocrystals defined as conjugated reticular oligomers (CROs, BBO-CRO$_{PDA}$, BBO-CRO$_{DHTA}$ and BBO-CRO$_{BPY}$, respectively). The BBO-CRO$_{PDA}$, BBO-CRO$_{DHTA}$, and BBO-CRO$_{BPY}$ exhibit a wider light-harvesting range spanning from ultraviolet to infrared regions and prolong the fluorescence lifetimes of photoinduced charge carriers compared with the counterpart bulk polymers of BBO-COF$_{PDA}$, BBO-COF$_{DHTA}$, and BBO-COF$_{BPY}$. The solution-processed BBO-CROs can be considered as a compelling "electronic paint" to fabricate large-area film on the flexible substrate, which is capable of preparing panel photoelectrodes for efficient solar/electron-to-hydrogen conversion. An illustrative representation of the whole procedure is depicted in Scheme 1. (i) Starting from the laboratory processing stage, the fabrication process involves the utilization of the spin-coating technique to fabricate thin-multilayer heterojunction photoelectrodes on an ITO substrate (2.0 × 2.0 cm). These devices incorporate both a hole transport layer (HTL) and an electron transport layer (ETL). The core segment of the photoactive layer is formed using a blended solution of BBO-CROs and the one-dimensional electron-donating polymer P27. (ii) Moving to the scale-up processing stage, we successfully utilized blade coating with colloidal BBO-CRO$_{BPY}$ as electronic inks on a flexible ITO substrate to prepare a large-scale 750 cm^2 photoelectrode, maintaining flexibility and enabling versatile applications in the field of flexible devices. Among them, the photoelectrode with an area of 100 cm^2 consisting of CuI/BBO-CRO$_{BPY}$+P27/SnO$_2$/Pt demonstrates a remarkable ΔJ value of 82.0 μA cm^{-2} and exhibits favorable stability. Our research not only marks a pivotal breakthrough in solution-processed COFs synthesis and processing techniques but also paves the way for novel avenues of application in PEC water reduction, particularly within the domain of flexible devices.

## 2. Experimental section

2.1. Materials

Reagents and solvents, readily available commercially, were utilized without additional purification. Detailed information on monomer synthesis is available in the Supporting Information.

2.2. Synthetic of bulk BBO-COFs

Synthetic of BBO-COF$_{PDA}$: In a Pyrex tube (volume of ca. 10 mL), 4,4',4'',4'''-(benzo[1,2-d:4,5-d′]bis(oxazole)−2,4,6,8-tetrayl)tetraaniline (BBO, 0.02 mmol, 10.5 mg) and terephthalaldehyde (0.04 mmol, 5.4 mg) were carefully weighed. The contents were dissolved in 2 mL of mesitylene/dioxane (17:3 v/v) and subjected to 5 minutes of sonication. Upon the addition of aqueous acetic acid (8 M, 0.2 mL), the solution underwent an additional 5 minutes of sonication to ensure even dispersion. The Pyrex tube underwent three freeze−pump−thaw cycles to remove gases, followed by flame-sealing. The sealed tube was then placed in an oven at 120 °C for 3 days.

After the allotted reaction time, the Pyrex tube was cooled to room temperature and opened. The resulting product was collected *via* centrifugation and subjected to cleaning steps involving DMF, ethanol, and acetone. The obtained powder was subsequently dried in a vacuum oven at 100 °C overnight.

Synthesis of BBO-COF$_{DHTA}$ and BBO-COF$_{BPY}$: The different linkers including DHTA and BPY were used in the synthesis process to yield BBO-COF$_{DHTA}$ and BBO-COF$_{BPY}$ by the same methods. (Details of
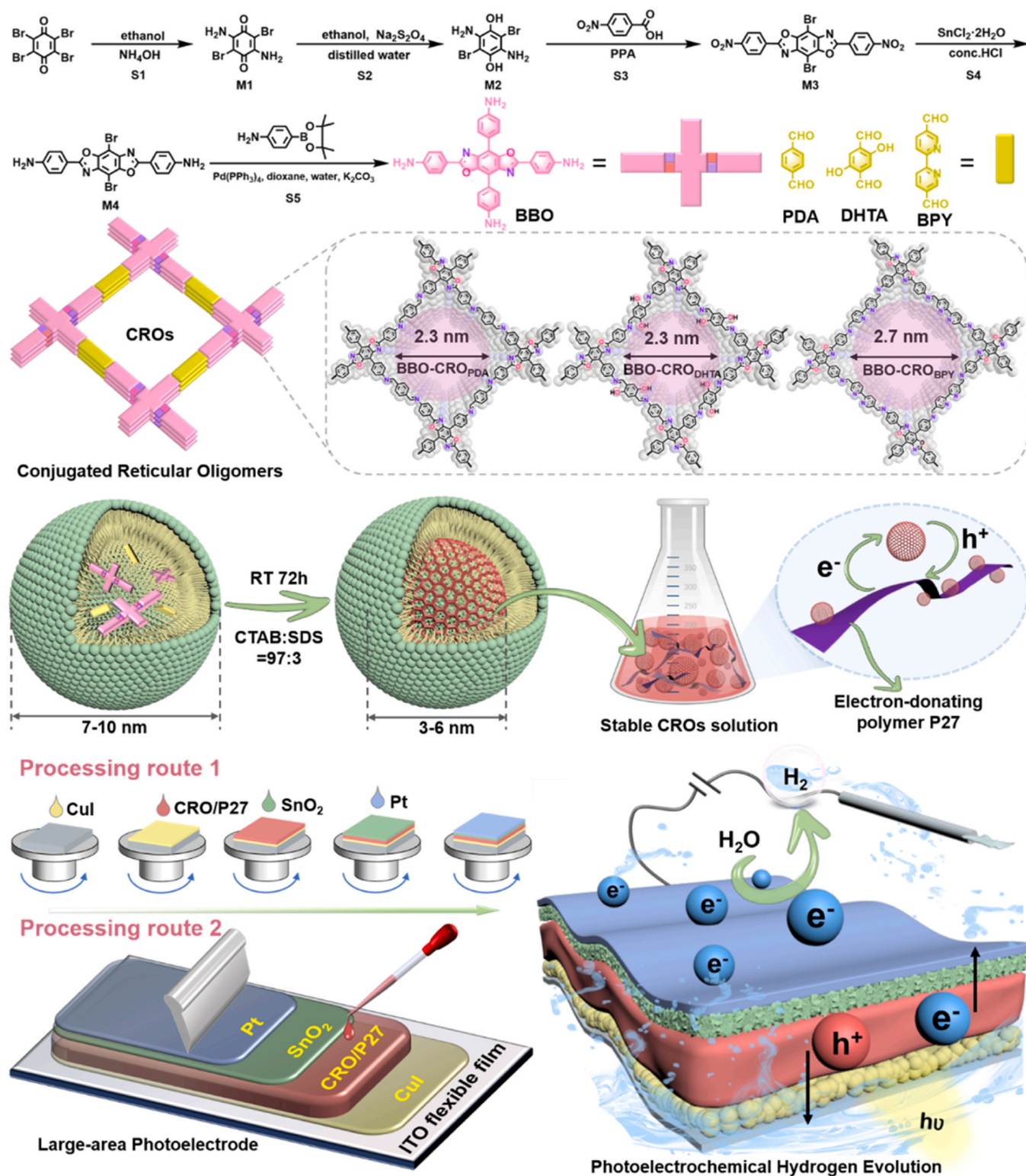
Scheme 1. Synthetic route of the monomer BBO and the process device diagram of BBO-CROs for PEC water splitting.

synthesized bulk BBO-COF$_{DHTA}$ and BBO-COF$_{BPY}$ in Supporting Information).

2.3. Synthetic of BBO-CRO$_{PDA}$, BBO-CRO$_{DHTA}$ and BBO-CRO$_{BPY}$

A solution of 4,4',4'',4'''-(benzo[1,2-d:4,5-d']bis(oxazole)−2,4,6,8-tetrayl)tetraaniline (0.02 mmol, 10.5 mg) in 1 mL of DMF was dropwise added to a CTAB aqueous solution (0.1 M, 58 mL) under ultrasonication. Subsequently, an aqueous solution of SDS (0.1 M, 1.8 mL) was introduced. Separately, terephthalaldehyde (0.04 mmol, 5.4 mg) was dissolved in 1 mL of DMF and added dropwise to another CTAB aqueous solution (0.1 M, 58 mL) under ultrasonication, followed by the addition of an aqueous solution of SDS (0.1 M, 1.8 mL). The resulting solutions were combined, and 5.8 mL of acetic acid was introduced to the mixture.

The reaction mixture was allowed to react at 30 °C for 3 days.

After the reaction, a mixture of ethanol (120 mL) and ammonia (28 %, 5.8 mL) was added to the micelle solution, and the mixture was allowed to stand for 48 hours until the upper solution became essentially colorless. The product was harvested through centrifugation and subjected to washing steps with ethanol and water. The resulting powder was then dried overnight in a freeze dryer under vacuum.

BBO-CRO$_{DHTA}$ and BBO-CRO$_{BPY}$ were obtained according to the same method. Refer to the Supporting Information for comprehensive details on the synthesis of BBO-CRO$_{DHTA}$ and BBO-CRO$_{BPY}$.

2.4. Material characterizations and PEC measurements

The comprehensive characterization of materials and detailed information on PEC testing can be found in the Supporting Information.

3. Results and discussion

3.1. Designed synthesis and characterizations of BBO-CROs

The BBO, which contains a benzoxazole unit, is distinguished by its exceptional combination of abundant active sites and superior photoelectric conversion efficiency [26,31]. We successfully synthesized the electron-donating BBO monomer through a series of five sequential chemical reactions (Please refer to the Supporting Information section for further details), then synthesized three stabilized colloidal solutions of BBO-CROs with a size below 5 nm through co-polycondensation of BBO with PDA, DHTA, and BPY in the catanionic micellar system, respectively. The micellar solution comprised anionic sodium dodecyl sulfate (SDS) and cationic hexadecyltrimethylammonium bromide (CTAB) surfactants, thereby forming a synergistic A+B system [32].
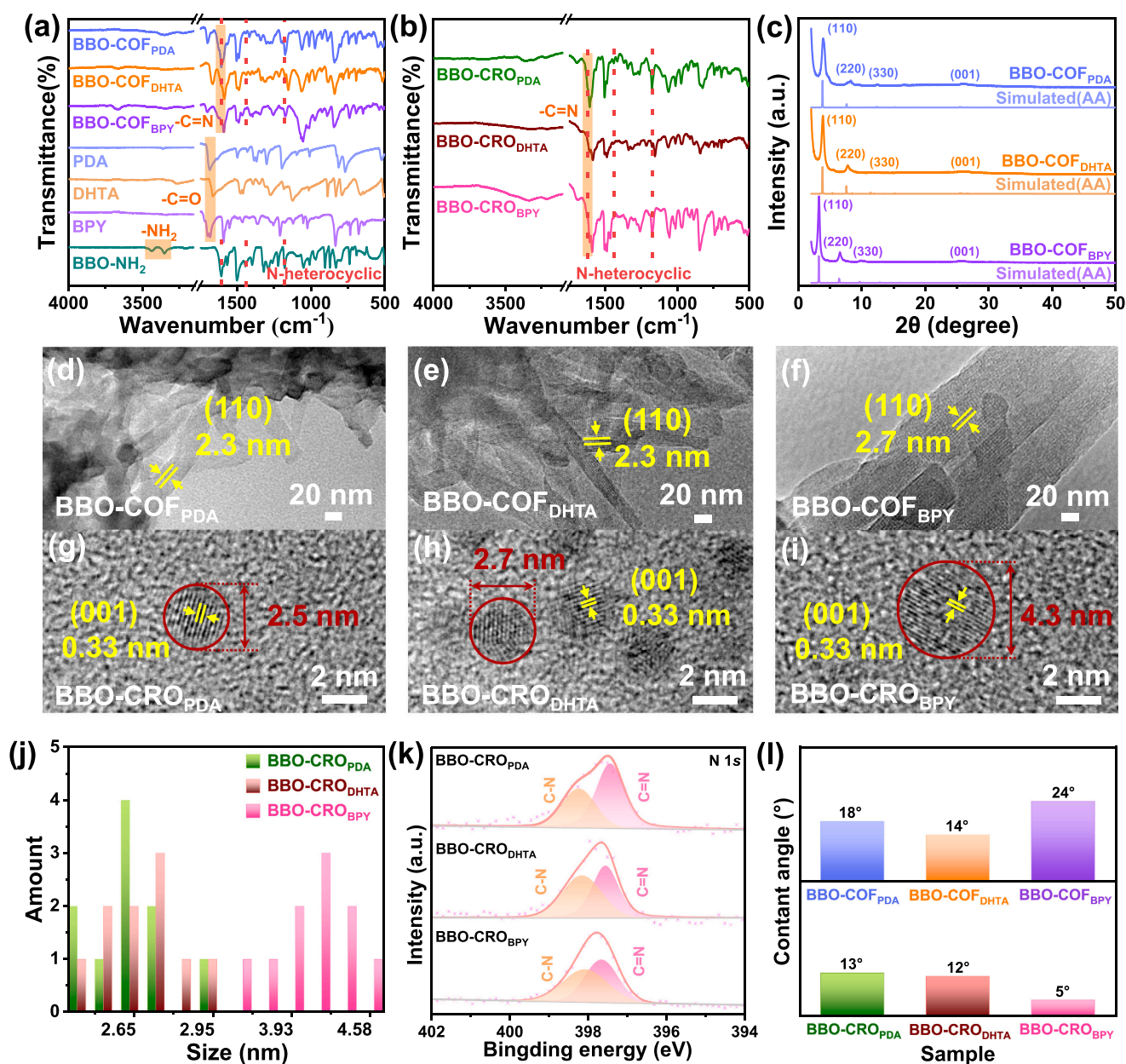
Fig. 1. FTIR spectra of (a) BBO-COF$_{PDA}$, BBO-COF$_{DHTA}$, and BBO-COF$_{BPY}$, and (b) BBO-CRO$_{PDA}$, BBO-CRO$_{DHTA}$, and BBO-CRO$_{BPY}$. (c) Simulated and experimental P-XRD pattern of BBO-COF$_{PDA}$, BBO-COF$_{DHTA}$, and BBO-COF$_{BPY}$. HR-TEM images of (d) BBO-COF$_{PDA}$, (e) BBO-COF$_{DHTA}$, (f) BBO-COF$_{BPY}$ and (g) BBO-CRO$_{PDA}$, (h) BBO-CRO$_{DHTA}$, and (i) BBO-CRO$_{BPY}$. (j) Size distributions of BBO-CRO$_{PDA}$, BBO-CRO$_{DHTA}$, and BBO-CRO$_{BPY}$ obtained from HR-TEM. (k) Deconvoluted N 1 s of BBO-CRO$_{PDA}$, BBO-CRO$_{DHTA}$, and BBO-CRO$_{BPY}$. (l) Contact angle of BBO-COF$_{PDA}$, BBO-COF$_{DHTA}$, BBO-COF$_{BPY}$, BBO-CRO$_{PDA}$, BBO-CRO$_{DHTA}$, and BBO-CRO$_{BPY}$.

Additionally, bulk BBO-COF$_{PDA}$, BBO-COF$_{DHTA}$, and BBO-COF$_{BPY}$ were synthesized *via* the solvothermal method for comparison.

The formation of bulk BBO-COF$_{PDA}$, BBO-COF$_{DHTA}$, and BBO-COF$_{BPY}$ were characterized by the Fourier transform infrared (FTIR) spectroscopy. In Fig. 1a, the characteristic signal of C=O and N–H stretching bands at 1661–1684 cm^{-1} and 3353–3441 cm^{-1} exhibit significant attenuation, while demonstrating the emergence of the distinctive signal corresponding to the C=N stretching vibration band at 1611–1623 cm^{-1}[27]. The FTIR spectra of BBO-COFs and BBO-CROs showed typical *N*-heterocyclic bands at 1624, 1439, and 1170 cm^{-1}, respectively, which are similar to those of the BBO-NH$_2$. Similarly, the presence of C=N stretching vibration bands at 1607 cm^{-1} in the FTIR spectra of BBO-CRO$_{PDA}$, BBO-CRO$_{DHTA}$, and BBO-CRO$_{BPY}$ (Fig. 1b) indicate successful polycondensation between monomers BBO and PDA, DHTA along with BPY.

The crystalline structures of the BBO-COF$_{PDA}$, BBO-COF$_{DHTA}$, and BBO-COF$_{BPY}$ were measured by powder X-ray diffraction (P-XRD). In Fig. 1c, BBO-COF$_{PDA}$ displays intense diffraction peaks at 3.9°, 8.3°, 12.5°, and 26.1°, which are assigned to the (110), (220), (330), and (001) crystallographic planes, respectively. BBO-COF$_{DHTA}$ exhibits diffraction peaks at 3.9°, 7.8°, 11.5°, and 26.2°, corresponding to the (110), (220), (330), and (001) facets. Similar results are observed for BBO-COF$_{BPY}$, which shows main reflection peaks at 3.3°, 6.5°, 9.9°, and 25.8°, which are attributable to (110), (220), (330), and (001) crystal facets, respectively. Furthermore, Pawley refinement was employed to analyze the experimental P-XRD data concerning the AA stacking models for the BBO-COF$_{PDA}$, BBO-COF$_{DHTA}$, and BBO-COF$_{BPY}$ samples (Fig. S1a−c). The simulated P-XRD patterns for the AA stacking configuration exhibit a remarkable concordance with the diffraction patterns acquired from the experimental analysis of BBO-COF$_{PDA}$, BBO-COF$_{DHTA}$, and BBO-COF$_{BPY}$. The Pawley refinement provides the cell parameters of $a = b = 32.99$ Å, $c = 3.50$ Å, $\alpha = \beta = \gamma = 90°$ for BBO-COF$_{PDA}$ with $R_{wp} = 4.92$ % and $R_p = 3.63$ %, respectively. The cell parameters of BBO-COF$_{DHTA}$ are $a = b = 33.06$ Å, $c = 3.50$ Å, $\alpha = \beta = \gamma = 90°$, with $R_{wp} = 4.31$ % and $R_p = 3.26$ %. Meanwhile, the cell parameters are $a = b = 38.95$ Å, $c = 3.50$ Å, $\alpha = \beta = \gamma = 90°$, with $R_{wp} = 4.92$ % and $R_p = 4.00$ % for BBO-COF$_{BPY}$.

The high-resolution transmission electron microscope (HR-TEM) images of BBO-COF$_{PDA}$, BBO-COF$_{DHTA}$, and BBO-COF$_{BPY}$ show clear lattice fringes measuring 2.3, 2.3, and 2.7 nm, respectively, corresponding to the long-order range channel (Fig. 1d−f). In the selected-area electron diffraction (SAED) in HR-TEM of BBO-COF$_{BPY}$, the diffraction spots align with a lattice distance of 0.7 nm, corresponding to the (440) facet (Fig. S2). It is indicated that BBO-COF$_{BPY}$ showcases remarkable crystal quality and exhibits a well-organized structure. As shown in Fig. 1g−i, BBO-CRO$_{PDA}$, BBO-CRO$_{DHTA}$, and BBO-CRO$_{BPY}$ exhibit notable characteristics of dispersion and uniformity. These BBO-CROs display a relatively uniform size distribution, with an average diameter of approximately 2.5, 2.7, and 4.3 nm, respectively (Fig. 1j), which was also confirmed using dynamic light scattering (DLS) analysis (Fig. S3). The HR-TEM images of BBO-CRO$_{PDA}$, BBO-CRO$_{DHTA}$, and BBO-CRO$_{BPY}$ unveil distinct lattice fringes with an interplanar spacing of 0.33 nm, corresponding to the (001) facet, which in accord with XRD results of BBO-COF$_{PDA}$, BBO-COF$_{DHTA}$, and BBO-COF$_{BPY}$. This indicates that BBO-CRO$_{PDA}$, BBO-CRO$_{DHTA}$, and BBO-CRO$_{BPY}$ possess a reticular nanocrystalline backbone.

The presence of carbon, nitrogen, and oxygen in BBO-COFs and BBO-CROs was confirmed by X-ray photoelectron spectroscopy (XPS) analysis, as shown in Fig. S4. The deconvoluted N 1*s* spectra of BBO-CRO$_{PDA}$, BBO-CRO$_{DHTA}$, and BBO-CRO$_{BPY}$ show two apparent peaks at 397.4±0.1 and 398.1±0.05 eV, which can be reasonably attributed to the chemical groups of C=N and C−N (Fig. 1k)[33]. This observation is consistent with the FTIR spectra results obtained for BBO-CRO$_{PDA}$, BBO-CRO$_{DHTA}$, and BBO-CRO$_{BPY}$, providing further evidence for the synthesis of BBO-CROs. Hydrophilicity plays a key role in promoting interfacial charge transfer and adsorption of water molecules in PEC

water reduction [34]. It is noteworthy to mention that BBO-COF$_{PDA}$, BBO-COF$_{DHTA}$, BBO-COF$_{BPY}$, BBO-CRO$_{PDA}$, BBO-CRO$_{DHTA}$, and BBO-CRO$_{BPY}$ were measured to have a small contact angle of 18°, 14°, 24°, 13°, 12°, and 5° (Fig. 1l and Fig. S7). The enhanced wettability is primarily attributed to the electronegative nature of N and O in BBO, enabling them to establish hydrogen bond interactions with water molecules [35].

To investigate the light-harvesting capacity and optical bandgap of BBO-COFs and BBO-CROs, ultraviolet-visible diffuse reflectance spectroscopy (UV–vis DRS) measurement was conducted. As depicted in Fig. 2a−c, the UV–vis DRS spectra reveal that both BBO-COFs and BBO-CROs exhibit absorption profiles from the ultraviolet to infrared regions. Notably, BBO-CRO$_{PDA}$, BBO-CRO$_{DHTA}$, and BBO-CRO$_{BPY}$ display a pronounced red shift relative to BBO-COF$_{PDA}$, BBO-COF$_{DHTA}$, and BBO-COF$_{BPY}$. The observed phenomenon can be ascribed to quantum size effects and *J-type* aggregation involving BBO chromophores among neighboring molecules [36], which give rise to modifications in the band structure and electronic state. The bandgap of BBO-CRO$_{BPY}$ is smaller than that of BBO-COF$_{BPY}$, as determined by Kubelka-Munk-transformed reflectance spectra. This discrepancy can be attributed to the enhanced intralayer charge transfer effect observed in BBO-CRO$_{BPY}$, which arises due to the shorter electron and hole transport paths within its lattice structure in comparison to that of bulk BBO-COF$_{BPY}$. Similar results are observed for BBO-CRO$_{PDA}$ and BBO-CRO$_{DHTA}$.

Upon exploring the transient photocurrent intensity of the BBO-COFs and BBO-CROs, it was found that BBO-CROs exhibited a notably greater photocurrent response than that of bulk BBO-COFs. This observation can potentially be attributed to the narrower band gap in BBO-CROs, which facilitates enhanced photon absorption and leads to the generation of a higher number of excited state carriers [37,38]. This conclusion is also confirmed by electron paramagnetic resonance (EPR) spectra of BBO-CROs. Both BBO-COFs and BBO-CROs displayed distinct EPR spectra with a prominent signal at $g = 2.004$, suggesting the existence of unpaired electrons [39]. The signal observed in BBO-CRO$_{PDA}$, BBO-CRO$_{DHTA}$, and BBO-CRO$_{BPY}$ is 2.4, 4.4, and 5.5 times greater than that of BBO-COF$_{PDA}$, BBO-COF$_{DHTA}$, BBO-COF$_{BPY}$, respectively. The significant disparity in signal intensity observed implies a higher concentration of unpaired electrons within the conduction band (CB) of BBO-CROs, indicating a potentially enhanced degree of electron delocalization or increased electron mobility in BBO-CROs [40]. The carrier transport was confirmed by electrochemical impedance spectroscopy (EIS). Nyquist plots showed that BBO-CROs have a smaller semicircle radius, suggesting that the charge-transfer resistance (R_{ct}) is lower than BBO-COFs, which is more beneficial to carrier transfer to the catalyst surface to participate in the water reduction reaction (Fig. S9). The R_{ct} exhibited a reduction for BBO-COFs and BBO-CROs upon exposure to visible light, which indicated that photo-induced charge carriers were generated under light irradiation. The findings underscore the distinctive electronic properties exhibited by BBO-CROs in comparison to BBO-COFs, thereby potentially impacting PEC water reduction involving charge transport and optoelectronic characteristics.

To elucidate the behavior of the photoinduced charge carriers, we employed a combination of steady-state and time-resolved photoluminescence (PL) techniques. Compared with BBO-COFs, BBO-CROs exhibit a distinct red shift in PL emission (Fig. S10). The molecular aggregations within BBO-CROs give rise to the formation of spherical or stacked structures, potentially resulting in modifications in charge redistribution and coupling [41]. In BBO-CROs, electrons and holes are more prone to localization, resulting in the formation of excitonic states. The establishment of excitonic states further affects the energy levels of both excited and emitted states, leading to the observed redshift phenomenon in the PL spectra of BBO-CROs. To elucidate the charge carrier lifetime in BBO-COFs and BBO-CROs, emission decay times were meticulously examined using biexponential decay kinetics. It is demonstrated that the fluorescence lifetimes of photoinduced charge carriers are prolonged on BBO-CRO$_{PDA}$ (3.08 ns), BBO-CRO$_{DHTA}$
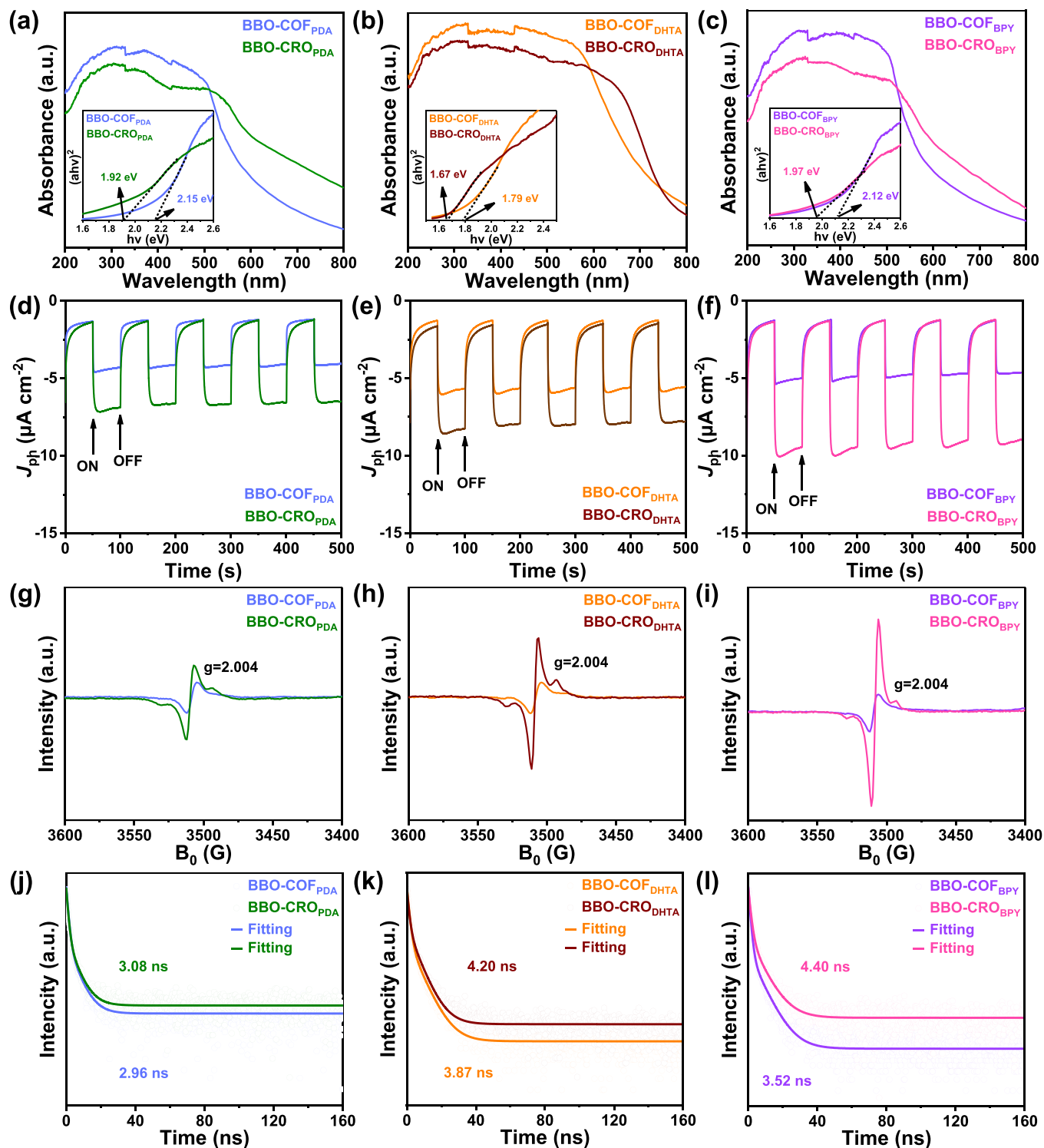
Fig. 2. UV–vis DRS spectra of (a) BBO-COF$_{PDA}$ and BBO-CRO$_{PDA}$, (b) BBO-COF$_{DHTA}$ and BBO-CRO$_{DHTA}$, and (c) BBO-COF$_{BPY}$ and BBO-CRO$_{BPY}$. Insets in (a), (b), and (c) are optical band gap calculations from Kubelka-Munk transformed reflectance spectra of BBO-COF$_{PDA}$ and BBO-CRO$_{PDA}$, BBO-COF$_{DHTA}$ and BBO-CRO$_{DHTA}$, BBO-COF$_{BPY}$ and BBO-CRO$_{BPY}$. Transient photocurrent measurement of (d) BBO-COF$_{PDA}$ and BBO-CRO$_{PDA}$, (e) BBO-COF$_{DHTA}$ and BBO-CRO$_{DHTA}$, and (f) BBO-COF$_{BPY}$ and BBO-CRO$_{BPY}$. EPR spectra of (g) BBO-COF$_{PDA}$ and BBO-CRO$_{PDA}$, (h) BBO-COF$_{DHTA}$ and BBO-CRO$_{DHTA}$, and (i) BBO-COF$_{BPY}$ and BBO-CRO$_{BPY}$. Time-resolved PL decay profiles of (j) BBO-COF$_{PDA}$ and BBO-CRO$_{PDA}$, (k) BBO-COF$_{DHTA}$ and BBO-CRO$_{DHTA}$, and (l) BBO-COF$_{BPY}$ and BBO-CRO$_{BPY}$.

(4.20 ns), and BBO-CRO$_{BPY}$ (4.40 ns) compared with corresponding BBO-COF$_{PDA}$ (2.96 ns), BBO-COF$_{DHTA}$ (3.87 ns), BBO-COF$_{BPY}$ (3.52 ns). For BBO-CROs, we observe a decrease in short-lived lifetimes due to bulk recombination and an increase in longer-lived lifetimes associated with surface recombination (Table S1). This intriguing phenomenon highlights the dynamic interplay between bulk and surface-related processes,

emphasizing the potential acceleration of bulk-to-surface electron transfer dynamics in BBO-CROs [42]. These findings provide valuable insights with far-reaching implications, suggesting enhanced utilization of photoinduced carriers in PEC water reduction.
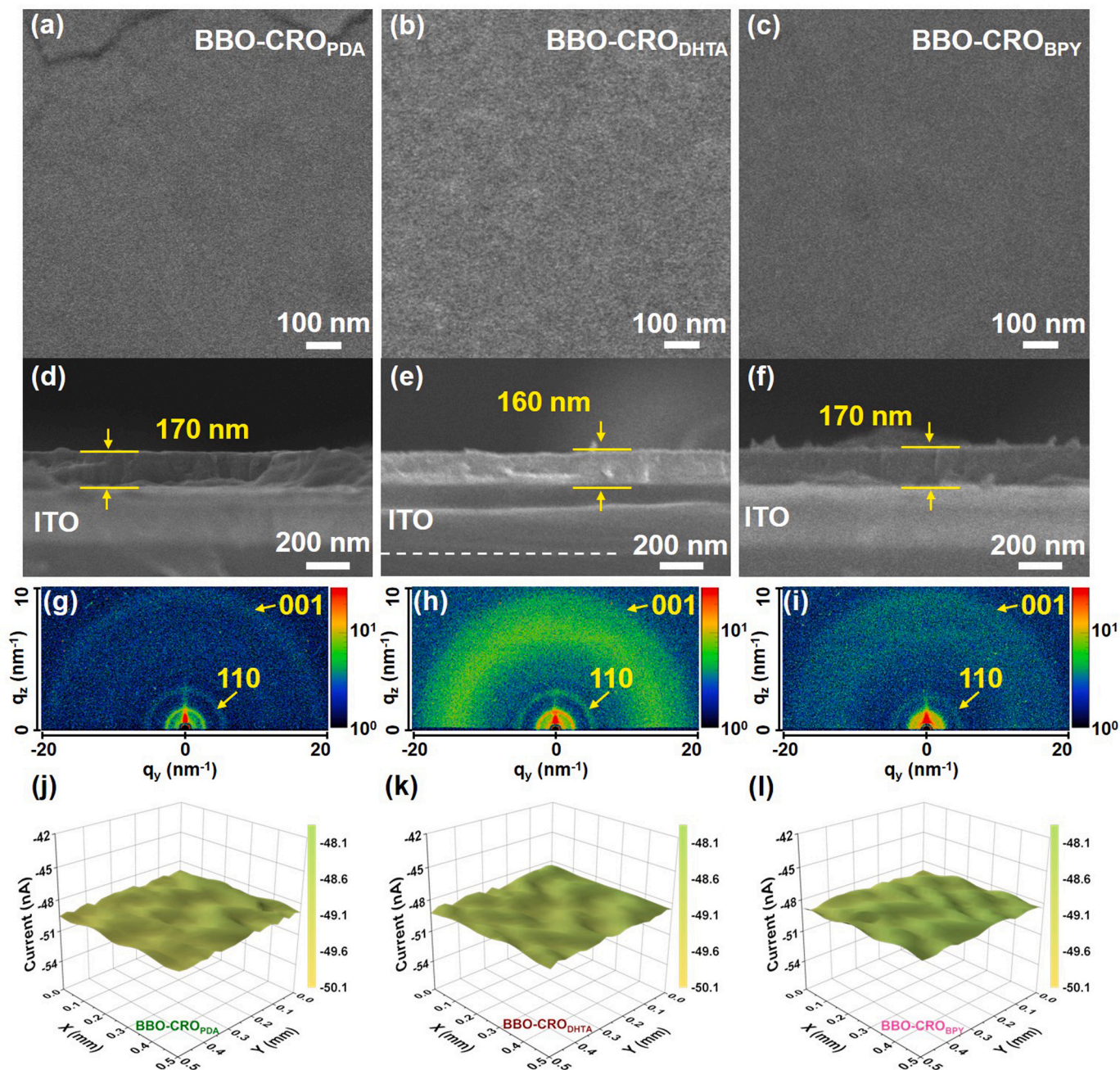
To observe the solution-processed BBO-CRO$_{PDA}$, BBO-CRO$_{DHTA}$, and BBO-CRO$_{BPY}$ films, we employed scanning electron microscopy (SEM) to

examine their morphologies fabricated *via* the spin-coating technique. It is observed that BBO-CRO$_{PDA}$, BBO-CRO$_{DHTA}$, and BBO-CRO$_{BPY}$ solution can obtain more consecutive and uniform nanomembranes on 2.0 × 2.0 cm ITO substrates (Fig. 3**a**−**c**) compared with the counterparts BBO-COF$_{PDA}$, BBO-COF$_{DHTA}$, BBO-COF$_{BPY}$ (Fig. S11). We also have conducted Atomic Force Microscopy (AFM) measurements on the BBO-CRO$_{PDA}$, BBO-CRO$_{DHTA}$, and BBO-CRO$_{BPY}$. Based on the AFM images in Fig. S12, the roughness of the spin-coated BBO-CRO$_{PDA}$, BBO-CRO$_{DHTA}$, and BBO-CRO$_{BPY}$ films was determined to be 2.6, 3.7, and 3.0 nm, respectively, indicating a relatively smooth and uniform surface. The SEM cross-sectional images reveal that the BBO-CRO$_{PDA}$, BBO-CRO$_{DHTA}$, and BBO-CRO$_{BPY}$ nanomembranes have a thickness of approximately 170, 160, and 170 nm, respectively. The exceptional film quality suggests

that colloid BBO-CROs can serve as an effective "electronic paint" material for large-area flexible PEC photoelectrodes fabrication.

Grazing-incidence wide-angle X-ray scattering (GIWAXS) imaging was employed to evaluate the crystallinity of BBO-CRO$_{PDA}$, BBO-CRO$_{DHTA}$, and BBO-CRO$_{BPY}$ membranes. As illustrated in Fig. 3g, the BBO-CRO$_{PDA}$ nanomembrane exhibits reflection peaks at q values of 2.7 and 18.2 nm^{-1}, corresponding to the (110) and (001) crystallographic planes, respectively. Fig. 3h displays analogous findings for the BBO-CRO$_{DHTA}$ nanomembrane, where two diffraction peaks are observed at 2.7 and 18.2 nm^{-1}, representing the (110) and (001) lattice planes. In Fig. 3i, the BBO-CRO$_{BPY}$ nanomembrane demonstrates reflection peaks at q values of 2.4 and 18.3 nm^{-1}, which are attributed to the (110) and (001) crystallographic planes, respectively. The results of GIWAXS

Fig. 3. Morphology of the solution-processed BBO-CRO$_{PDA}$, BBO-CRO$_{DHTA}$, and BBO-CRO$_{BPY}$ nanomembranes. Top−down SEM morphology of spin-coated (a) BBO-CRO$_{PDA}$, (b) BBO-CRO$_{DHTA}$, and (c) BBO-CRO$_{BPY}$. Cross-sectional SEM images of (d) ITO/BBO-CRO$_{PDA}$, (e) ITO/BBO-CRO$_{DHTA}$, and (f) ITO/BBO-CRO$_{BPY}$ with 4 spin-coating cycles. Two-dimensional GIWAXS patterns of (g) BBO-CRO$_{PDA}$, (h) BBO-CRO$_{DHTA}$, and (i) BBO-CRO$_{BPY}$. SECM images of (j) BBO-CRO$_{PDA}$, (k) BBO-CRO$_{DHTA}$, and (l) BBO-CRO$_{BPY}$.

indicate that the well-defined nanocrystals of BBO-CRO$_{PDA}$, BBO-CRO$_{DHTA}$, and BBO-CRO$_{BPY}$ exhibit well film-processing ability.

We used the scanning electrochemical microscopy (SECM) in feedback mode to evaluate the hyperfine photoelectric structure of the active layer. This sophisticated approach involved meticulously adjusting the probe distance to bring it near the BBO-CRO$_{PDA}$, BBO-CRO$_{DHTA}$, and BBO-CRO$_{BPY}$ surface without making actual physical contact. The probe was fixed at a specific height and conducted planar scans in both the X−Y directions, effectively covering an area measuring 0.5×0.5 mm. Simultaneously, we meticulously monitored the current variations at various positions across the surface. As depicted in Fig. 3 j−l, our findings revealed that the current fluctuations observed on the BBO-CRO$_{PDA}$, BBO-CRO$_{DHTA}$, and BBO-CRO$_{BPY}$ surfaces remained consistently within an extremely narrow range, measuring from 48 to 50 nA. This observation signifies the presence of steady-state tip currents. The remarkably stable current can be attributed to the continuity and uniformity of the BBO-CRO$_{PDA}$, BBO-CRO$_{DHTA}$, and BBO-CRO$_{BPY}$ films. These results provide compelling evidence for the investigated layers' exceptional surface quality and flatness, highlighting their suitability for advanced PEC water reduction.

3.2. PEC water reduction performance of heterojunction devices

After investigating the morphology of BBO-CRO$_{PDA}$, BBO-CRO$_{DHTA}$, and BBO-CRO$_{BPY}$ nanomembranes, we considered applying them as photocathodes in PEC water reduction. The conduction band minimum (CBM) and valance band maximum (VBM) of BBO-CRO$_{PDA}$, BBO-CRO$_{DHTA}$, and BBO-CRO$_{BPY}$ are shown in Fig. S14, which exhibit thermodynamic compatibility with the hydrogen evolution reaction (HER) [43]. The PEC performance in this work was evaluated using a three-electrodes setup in an aqueous solution of Na$_2$SO$_4$ (0.1 mol L^{-1}, pH = 7) without the presence of a sacrificial agent. The photocathodes fabricated by directly spin coating the solution of BBO-CRO$_{PDA}$, BBO-CRO$_{DHTA}$, and BBO-CRO$_{BPY}$ on ITO substrate demonstrated photocurrent response under simulated sunlight illumination, as evidenced by the linear sweep voltammetry (LSV) results shown in Fig. S15 and Fig. S16, which confirming their feasibility for PEC water reduction.

In pursuit of enhancing the photocurrent response and advancing the application of COFs in PEC water reduction, a comprehensive investigation included introducing a hole-transport layer (HTL) and establishing a heterojunction was undertaken. Vapor-deposited CuI was employed as an HTL to improve the efficiency of PEC heterojunction devices due to its exceptional electron mobility and cost-effectiveness [44]. Additionally, as firmly established within the realm of organic electronics, when an electron-donating OSs interfaces with an electron-accepting OSs to create a bulk heterojunction (BHJ) architecture, an augment of interfaces for a highly efficient generation and separation of free charge carriers could be achieved, potentially leading to an increased photocurrent [45,46]. This phenomenon can be readily fine-tuned by altering the pairing of the donor and acceptor OSs [47]. Herein, as shown in Fig. S17a, we have specially designed and synthesized a donor polymer coded as P27, with the benzothiadiazole units serving as the electron-donating component actively involved in electron transport. Through the strategic introduction of chlorine atoms into the π-bridge thiophene segment of the polymer, we have achieved a significant reduction highest occupied molecular orbital (HOMO) energy level of the polymer. This deliberate reduction in the HOMO energy level substantially augments the electron affinity of P27, rendering it highly conducive to electron transfer. This consideration is crucial since the photovoltage correlates directly with the energy offset between the lowest unoccupied molecular orbital (LUMO) level of an acceptor and the HOMO level of a donor [13]. We constructed BHJ architecture using BBO-CROs and 1D electron-donating polymer P27, defined as BBO-CROs+P27. The energy levels of P27, BBO-CRO$_{PDA}$, BBO-CRO$_{DHTA}$, and BBO-CRO$_{BPY}$ are illustrated in Fig. S17d. It is evident that the donor polymer P27 facilitates charge transfer to the acceptor BBO-CROs by

supplying electrons, thereby mitigating the energy level disparity, and promoting electron flow from P27 to BBO-CROs, ultimately enabling current generation.

Mott-Schottky analysis was conducted to determine the charge carrier densities for PEC. The slope of the Mott-Schottky plot is inversely proportional to charge carrier densities [48]. Therefore, a smaller slope indicates higher charge carrier densities and faster charge transfer kinetics during the PEC process. BBO-CRO$_{PDA}$, BBO-CRO$_{DHTA}$, and BBO-CRO$_{BPY}$ exhibit the slope of 2.56, 2.71, and 2.60, which is smaller than the corresponding BBO-COF$_{PDA}$ (3.04), BBO-COF$_{DHTA}$ (2.89) and BBO-COF$_{BPY}$ (2.62), respectively. The presence of non-symmetric BBO structures in small-molecular BBO-CROs may induce an electron density enhancement effect. This may imply that within the BBO-CRO structures, electrons tend to concentrate more in regions exhibiting asymmetry. BBO-CROs possess shorter electron transfer pathways compared with bulk BBO-COFs. The smaller dimensions of BBO-CRO nanocrystals result in shorter distances that electrons need to travel, which in turn reduces electron transfer resistance. These shorter electron transfer pathways allow electrons to flow more rapidly toward catalytic sites or photoelectrodes, further enhancing electrocatalytic efficiency. In addition, BBO-CRO$_{PDA}$+P27, BBO-CRO$_{DHTA}$+P27, and BBO-CRO$_{BPY}$+P27 exhibit the least slope among BBO-CRO$_{PDA}$, BBO-CRO$_{DHTA}$, and BBO-CRO$_{BPY}$-based photoelectrodes, respectively, as illustrated in Fig. S18. It is suggested that BHJ device configuration generates abundant charge carriers, which play a crucial role in enhancing the performance of PEC.

The heterojunction device comprising CuI and BBO-CROs+P27 is observed to positively shift the onset potential (Fig. 4a−c), indicating that the BBO-CROs+P27 heterojunction facilitates efficient charge separation. CuI and CuI/P27 only show a current difference (ΔJ) between photocurrent and dark current of 0.9 and 6.1 μA cm^{-2} (Fig. S19), while the ΔJ of CuI/BBO-CRO$_{PDA}$, CuI/BBO-CRO$_{DHTA}$, and CuI/BBO-CRO$_{BPY}$ are measured to be 7.6, 9.7, and 21.2 μA cm^{-2} at 0.4 V *vs.* RHE. It is noteworthy that the ΔJ of CuI/BBO-CRO$_{PDA}$+P27, CuI/BBO-CRO$_{DHTA}$+P27, and CuI/BBO-CRO$_{BPY}$+P27 are 20.4, 24.4, and 27.2 μA cm^{-2} at 0.4 V *vs.* RHE, which is 51.0, 20.3 and 27.2 times higher than that of BBO-COF$_{PDA}$, BBO-COF$_{DHTA}$, and BBO-COF$_{BPY}$. It is suggested that the provided photocathode architecture appears to be a promising strategy for improving charge separation within COFs. The key factor responsible for this enhanced performance lies in the more favorable thermodynamics governing the transfer of photogenerated holes towards the P27 donor polymer layer positioned at the interface of the BBO-CROs+P27 heterojunction.

In order to transfer photogenerated electrons to photoelectrode and balance the electron/hole transfer process, we introduced SnO$_2$ as an electron transfer layer (ETL) into the PEC water reduction device. While CuI/BBO-CRO$_{PDA}$+P27, CuI/BBO-CRO$_{DHTA}$+P27, and CuI/BBO-CRO$_{BPY}$+P27 exhibit an increased dark current at 0.4 V *vs.* RHE, the introduction of a SnO$_2$ layer atop BBO-CRO$_{PDA}$+P27, BBO-CRO$_{DHTA}$+P27, and BBO-CRO$_{BPY}$+P27 as an electron-collecting layer results in reduced dark current and a further enhancement in ΔJ within CuI/BBO-CRO$_{PDA}$+P27/SnO$_2$, CuI/BBO-CRO$_{DHTA}$+P27/SnO$_2$, and CuI/BBO-CRO$_{BPY}$+P27/SnO$_2$ (Table S2−4). This may be attributed to the SnO$_2$ layer providing an efficient pathway for electron conduction, thereby minimizing electron recombination and leakage, ultimately leading to improved photoelectric conversion efficiency [49,50]. Additional investigations were conducted to advance the realization of PEC water reduction. To furnish catalytically active sites for the HER, Pt nanoparticles were incorporated as an HER catalyst overlay onto BBO-CRO$_{PDA}$+P27, BBO-CRO$_{DHTA}$+P27, and BBO-CRO$_{BPY}$+P27. Full details and discussions regarding optimizing the device structure are provided in Fig. S20. As shown in Fig. 4a−c, the optimized photoelectrodes with the structure of CuI/BBO-CRO$_{PDA}$+P27/SnO$_2$/Pt, CuI/BBO-CRO$_{DHTA}$+P27/SnO$_2$/Pt, and CuI/BBO-CRO$_{BPY}$+P27/SnO$_2$/Pt result in ΔJ of 47.5, 72.3, and 86.5 μA cm^{-2} at 0.4 V *vs.* RHE, which is 118.8, 60.3 and 86.5 times higher than that of BBO-COF$_{PDA}$,
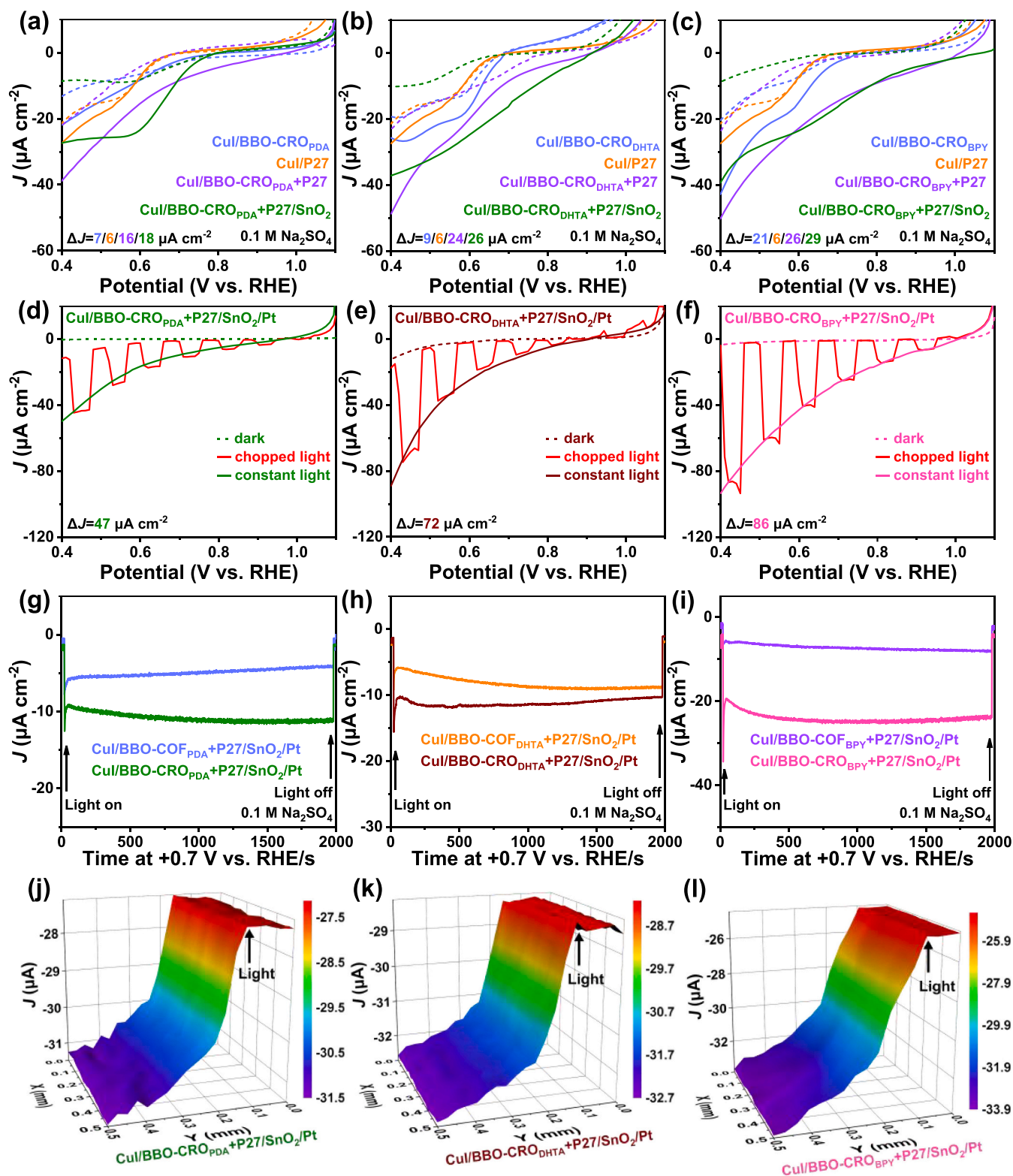
Fig. 4. (a) LSV curves of CuI/P27, CuI/BBO-CRO$_{PDA}$, CuI/BBO-CRO$_{PDA}$+P27, and CuI/BBO-CRO$_{PDA}$+P27/SnO$_2$. (b) LSV curves of CuI/P27, CuI/BBO-CRO$_{DHTA}$, CuI/BBO-CRO$_{DHTA}$+P27, and CuI/BBO-CRO$_{DHTA}$+P27/SnO$_2$. (c) LSV curves of CuI/P27, CuI/BBO-CRO$_{BPY}$, CuI/BBO-CRO$_{BPY}$+P27, and CuI/BBO-CRO$_{BPY}$+P27/SnO$_2$. LSV curves of (d) CuI/BBO-CRO$_{PDA}$+P27/SnO$_2$/Pt, (e) CuI/BBO-CRO$_{DHTA}$+P27/SnO$_2$/Pt, and (f) CuI/BBO-CRO$_{BPY}$+P27/SnO$_2$/Pt under constant and chopped light. CA curves of (g) CuI/BBO-CRO$_{PDA}$+P27/SnO$_2$/Pt, (h) CuI/BBO-CRO$_{DHTA}$+P27/SnO$_2$/Pt and (i) CuI/BBO-CRO$_{BPY}$+P27/SnO$_2$/Pt. SECM images of (j) CuI/BBO-CRO$_{PDA}$+P27/SnO$_2$/Pt, (k) CuI/BBO-CRO$_{DHTA}$+P27/SnO$_2$/Pt, and (l) CuI/BBO-CRO$_{BPY}$+P27/SnO$_2$/Pt.

BBO-COF$_{DHTA}$, and BBO-COF$_{BPY}$. The enhanced photocurrent is credited to establishing a built-in electric field within the heterojunction photo-electrode, adeptly suppressing charge recombination at the hetero-junction interface [51]. The results of chronoamperometry (CA) measurements, as illustrated in Fig. 4g−i, demonstrate that the optimal photocathodes exhibit exceptional stability by maintaining continuous operation at +0.7 *vs.* RHE for over 50 minutes.

Furthermore, we provided electrochemical active area (ECSA), incident-photon-to-current efficiency (IPCE), and Faradaic efficiency to facilitate a fair comparison in ITO/CuI/BBO-CRO$_{PDA}$+P27/SnO$_2$/Pt, ITO/CuI/BBO-CRO$_{DHTA}$+P27/SnO$_2$/Pt, and ITO/CuI/BBO-CRO$_{BPY}$+P27/SnO$_2$/Pt photoelectrodes. ECSA is an important parameter to characterize the catalytic activity and has a direct linear relationship with the double-layer capacitance (C_{dl}). C_{dl} was also measured to evaluate the ECSA of BBO-COFs and BBO-CROs by CV in the non-faradic region of 1.21−1.31 V *vs.* RHE. The values of C_{dl} were calculated as 0.18, 0.22, 0.23, 0.43, 0.48, and 0.50 mF cm^{-2} for BBO-COF$_{PDA}$, BBO-COF$_{DHTA}$, BBO-COF$_{BPY}$, BBO-CRO$_{PDA}$, BBO-CRO$_{DHTA}$ and BBO-CRO$_{BPY}$ (Fig. S21). The higher C_{dl} catalyst can provide a high reaction site density for adsorption, which is conducive to effective charge transfer [52].

The IPCE is a key descriptor for evaluating the light utilization efficiency of photoelectrodes. We tested the IPCE to assess the intrinsic PEC performance of photoelectrodes. As shown in Fig. S22, the peak IPCE value of BBO-CRO$_{PDA}$, BBO-CRO$_{DHTA}$, and BBO-CRO$_{BPY}$ is as large as 0.51 % (at 550 nm), 0.63 % (at 550 nm), 0.72 % (at 520 nm). Especially, the IPCE of BBO-CRO$_{BPY}$ is significantly higher than that of reported COFs' photocathodes, such as BDT-ETTA COFs (~0.04 % at 520 nm) [53], CRO-TtzTp-Cg (~0.45 % at 520 nm), CRO-BtzTp-Cg (~0.44 % at 520 nm), CRO-TtzTp (~0.38 % at 520 nm) and CRO-BtzTp (~0.33 %) [54].

A continuous 5 h electrolysis was carried out in PEC cell using ITO/CuI/BBO-CRO$_{PDA}$+P27/SnO$_2$/Pt, ITO/CuI/BBO-CRO$_{DHTA}$+P27/SnO$_2$/Pt, and ITO/CuI/BBO-CRO$_{BPY}$+P27/SnO$_2$/Pt as photoanodes, respectively (Fig. S23). The evolved H$_2$ amounts of ITO/CuI/BBO-CRO$_{PDA}$+P27/SnO$_2$/Pt, ITO/CuI/BBO-CRO$_{DHTA}$+P27/SnO$_2$/Pt, and ITO/CuI/BBO-CRO$_{BPY}$+P27/SnO$_2$/Pt photoelectrodes is 8.7, 13.8, and 20.6 μmol cm^{-2} after 5 h, respectively. Additionally, the Faradic efficiency of H$_2$ is calculated to be over 90 % in ITO/CuI/BBO-CRO$_{PDA}$+P27/SnO$_2$/Pt, ITO/CuI/BBO-CRO$_{DHTA}$+P27/SnO$_2$/Pt, and ITO/CuI/BBO-CRO$_{BPY}$+P27/SnO$_2$/Pt photoelectrodes, demonstrating that the photogenerated electrons almost participate in the PEC water reduction reaction.

We employed SECM to investigate the localized PEC activity of the photoelectrodes in the dark and with light irradiation (Fig. 4j−l). The photocatalytic activity of the CuI/BBO-CRO$_{PDA}$+P27/SnO$_2$/Pt, CuI/BBO-CRO$_{DHTA}$+P27/SnO$_2$/Pt, and CuI/BBO-CRO$_{BPY}$+P27/SnO$_2$/Pt photoelectrodes were monitored in real-time through an in-situ approach using the generation–collection mode with a redox couple. The CuI/BBO-CRO$_{PDA}$+P27/SnO$_2$/Pt, CuI/BBO-CRO$_{DHTA}$+P27/SnO$_2$/Pt, and CuI/BBO-CRO$_{BPY}$+P27/SnO$_2$/Pt photoelectrodes exhibited dark currents of 27.3, 28.2, and 24.5 μA, respectively. These dark current measurements demonstrated stable profiles, underscoring the consistent nature of the photoelectrode surfaces. Furthermore, the photocurrent generated by these photoelectrodes was observed to be 31.4, 32.7, and 33.9 μA for CuI/BBO-CRO$_{PDA}$+P27/SnO$_2$/Pt, CuI/BBO-CRO$_{DHTA}$+P27/SnO$_2$/Pt, and CuI/BBO-CRO$_{BPY}$+P27/SnO$_2$/Pt, respectively. The CuI/BBO-CRO$_{PDA}$+P27/SnO$_2$/Pt, CuI/BBO-CRO$_{DHTA}$+P27/SnO$_2$/Pt, and CuI/BBO-CRO$_{BPY}$+P27/SnO$_2$/Pt photoelectrodes generate electron-hole pairs under light irradiation, a fundamental process in PEC. This phenomenon increases the population of electrons available for participation in the reduction of a redox mediator. As a direct result of this enhanced electron availability, there is a noticeable improvement in the tip photocurrent response. The intensive photocurrent can be attributed to an increase in the generation of photogenerated charge carriers, which in turn leads to an increased electron concentration within the electron transport layer of the photoelectrodes. This surplus of electrons can efficiently transfer to the catalytic layer, significantly enhancing the efficiency of electron transfer processes. These photogenerated charge carriers possess the ability to move freely within the photoelectrodes when driven by an external circuit. This mobility provides an ample supply of additional electrons and holes for catalytic reactions, ultimately contributing to the overall enhancement of the photocatalytic activity of the photoelectrodes. Moreover, the photocurrent of CuI/BBO-CRO$_{PDA}$+P27/SnO$_2$/Pt, CuI/BBO-CRO$_{DHTA}$+P27/SnO$_2$/Pt, and CuI/BBO-CRO$_{BPY}$+P27/SnO$_2$/Pt reaches 2.8, 6.7, and 2.5 times than that of CuI/BBO-CRO$_{PDA}$/SnO$_2$/Pt, CuI/BBO-CRO$_{DHTA}$/SnO$_2$/Pt, and CuI/BBO-CRO$_{BPY}$/SnO$_2$/Pt. This further underscores the pivotal role of P27 in enhancing photocurrent. Incorporating P27 into a BHJ structure provides an efficient electron transport pathway, fine-tunes energy level matching for improved electron transfer, expedites rapid charge separation, and amplifies light absorption, ultimately resulting in an increased yield of photogenerated electrons.

3.3. Mechanism investigation

To gain a deeper understanding of electron excitation in benzoxazole and its intrafragment charge redistribution and interfragment charge transfer, we performed calculations of the charge transfer spectrum using time-dependent density functional theory (TD-DFT) in conjunction with Multiwfn software [55,56]. As shown in Fig. 5a−c, using this approach, we investigated the individual contributions of intrafragment electron redistributions and interfragment electron transfers to the absorption spectra of BBO-CRO$_{PDA}$, BBO-CRO$_{DHTA}$, and BBO-CRO$_{BPY}$. Except for the prominent electron transfer feature at around 435 nm, indicative of electron transfer from benzoxazole to PDA, the data demonstrate (2→1), that nearly the entire optical absorption spectrum of BBO-CRO$_{PDA}$ primarily arises from electron transitions within the benzoxazole component. This assertion is substantiated by the remarkable proximity between the red curve representing electron redistribution within the benzoxazole fragment and the absorption spectrum (depicted by the purple curve) of the BBO-CRO$_{PDA}$. It is noteworthy that the contribution of electron transfer to PDA in the direction of benzoxazole surpasses that of electron transfer to PDA in the direction of the benzene ring (2→3). This phenomenon can be attributed to the higher electron affinity of the benzoxazole unit, leading to an uneven distribution of electron density in BBO-CRO$_{PDA}$. Electrons exhibit a greater tendency to delocalize within the benzoxazole unit and subsequently transfer to PDA. As seen in Fig. 5d, the corresponding isosurface map of hole and electron distributions for BBO-CRO$_{PDA}$ exhibits electrons are concentrated on the benzoxazole unit. This facilitated electron transport enhances the delocalization of π electrons in BBO-CRO$_{PDA}$, thereby prolonging the residence time of photoexcited electrons at the catalytic interface and consequently augmenting their likelihood to participate in the PEC water reduction. The asymmetry of the benzoxazole structure effectively mitigates electron backflow, thereby enhancing the separation efficiency of electrons and holes in PEC water reduction devices. Similar results can be seen in BBO-CRO$_{DHTA}$ and BBO-CRO$_{BPY}$.

We delved into the potential electronic excitation transitions within the systems BBO-CRO$_{PDA}$, BBO-CRO$_{DHTA}$, and BBO-CRO$_{BPY}$, including local excitation and charge transfer mode. To differentiate between these two modes, we relied on the S/D value, where "S" denotes the calculated overlap integral of the hole-electron distribution, and "D" represents the calculated distance between the centroids of the hole and the electron. A smaller "S" value coupled with a larger "D" value signifies a more pronounced charge transfer process as per the hole-electron theory [57–59]. After the calculations, we determined the S/D values for BBO-CRO$_{PDA}$, BBO-CRO$_{DHTA}$, and BBO-CRO$_{BPY}$, and they exhibited the following decreasing order: BBO-CRO$_{PDA}$ (0.028), BBO-CRO$_{DHTA}$ (0.022), and BBO-CRO$_{BPY}$ (0.020). This trend suggests that among these systems, BBO-CRO$_{BPY}$ exhibits the most favorable conditions for charge transfer.
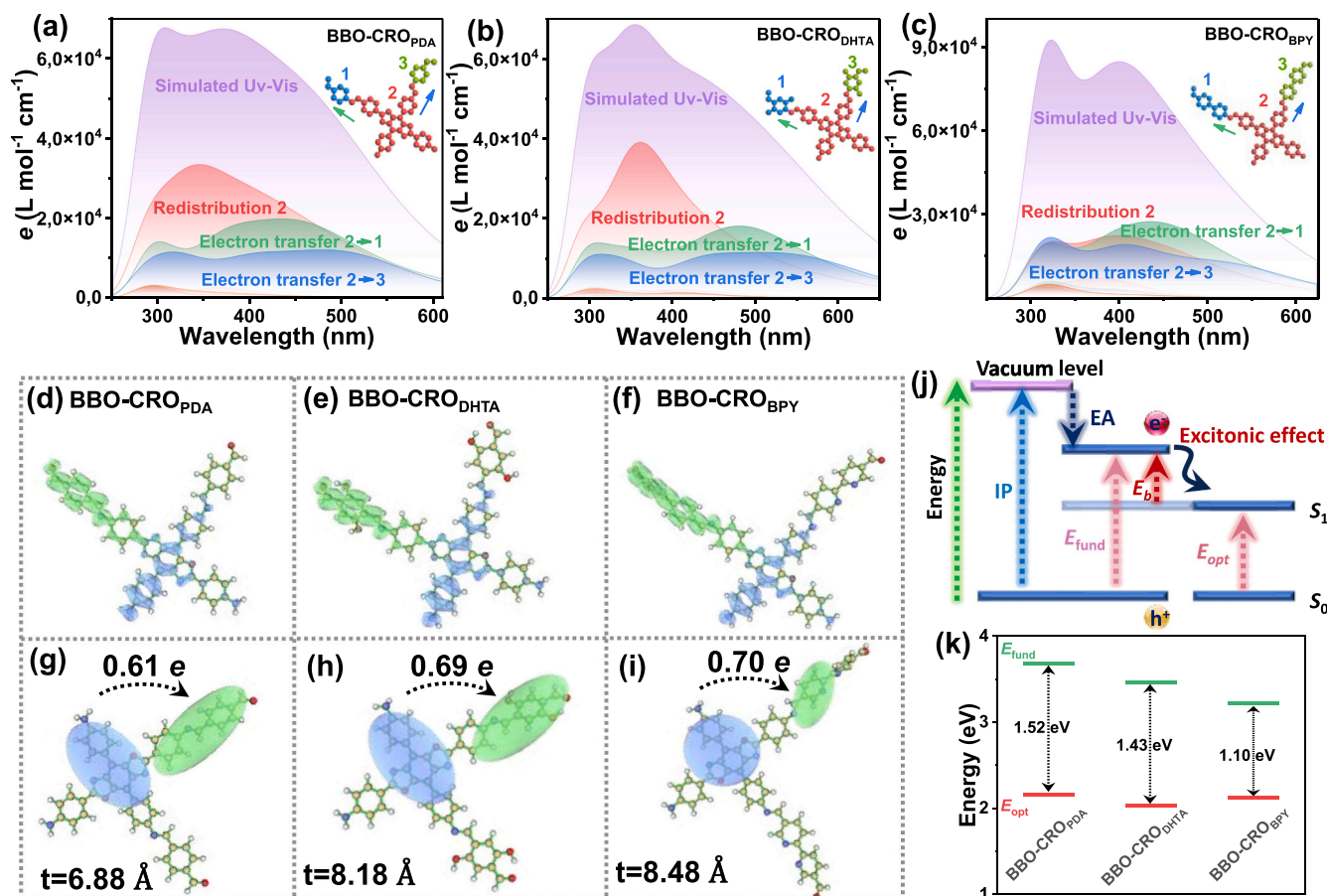
Fig. 5. The electronic absorption spectrum and charge-transfer spectrum (CTS) (a) BBO-CRO$_{PDA}$, (b) BBO-CRO$_{DHTA}$, and (c) BBO-CRO$_{BPY}$. Isosurface map of hole and electron distributions for (d) BBO-CRO$_{PDA}$, (e) BBO-CRO$_{DHTA}$, and (f) BBO-CRO$_{BPY}$. Isosurface map of centroids of charges for (g) BBO-CRO$_{PDA}$, (h) BBO-CRO$_{DHTA}$, and (i) BBO-CRO$_{BPY}$. (j) Illustration of various energy gaps in the molecular base: S_0 and S_1 denote the electronic ground state and the lowest excited state, respectively. IP: ionization potential; EA: electron affinity; E_{fund}: fundamental gap; E_{opt}: optical gap; E_b: exciton binding energy. (k) Calculated exciton binding energy for BBO-CRO$_{PDA}$, BBO-CRO$_{DHTA}$, and BBO-CRO$_{BPY}$.

In addition, we explored the extent of orbital overlap between the orbitals and the distance to the centroids within D−A pairs between the building block BBO and the aldehyde-based modules including PDA, DHTA, and BPY. Based on a more intuitive representation of charge centroids, the electron and hole centroids for D−A pairs are observed to be located on the BBO- and aldehyde-based modules segments, respectively, thereby demonstrating their roles as electron donor and acceptor following the aforementioned energy level calculations. To investigate the subtle changes in BBO-CRO$_{PDA}$, BBO-CRO$_{DHTA}$, and BBO-CRO$_{BPY}$, we quantified the degree of separation between holes and electrons (*t* index) by analyzing variations in electron density and calculating the amount of transferred electrons during electron excitation (Fig. 5**g**−**i**). Among BBO-CRO$_{PDA}$, BBO-CRO$_{DHTA}$, and BBO-CRO$_{BPY}$, BBO-CRO$_{BPY}$ exhibits the largest *t* index (8.48 Å) and the greatest amount of transferred electrons (0.70 e). It is implied that BBO-CRO$_{BPY}$ features the superior D−A interaction, inferring the most excellent photocurrent among the materials studied. To validate this conclusion, the exciton binding energy (E_b) was calculated as a descriptor of the excitonic effect. The E_b is calculated by the formula:

$$E_b = E_{fund} - E_{opt}$$

where E_{fund} is the fundamental gap and is defined as the difference between ionization potential (IP) and electron affinity (EA), and E_{opt} is the optical gap and is defined as the difference between the ground state and the lowest excited state (Fig. 5**j**) [60]. The results demonstrate a descending order of BBO-CRO$_{PDA}$ > BBO-CRO$_{DHTA}$ > BBO-CRO$_{BPY}$,

which aligns with the trend observed in the S/D values (Fig. 5**k**). Considering the kinetic behavior of excitons, a lower E_b indicates enhanced ease of exciton dissociation and efficient separation of electron-hole pairs.

3.4. Large-area panel photoelectrodes for PEC devices

To achieve commercialized preparation, we used the blade coating method to prepare large-area panel electrodes on the flexible ITO substrate using BBO-CRO$_{BPY}$ electronic paint for PEC water reduction. Through this method, we have successfully fabricated a large-scale photoelectrode with an area of 750 cm^2, while preserving its flexibility and bendability, thus offering significant prospects for versatile applications in the field of flexible devices (Fig. 6**a**). The exceptional photoelectrochemical performance initially demonstrated on a small-scale photoelectrode with a size of 2.0 × 2.0 cm remained potential photoelectrochemical activity upon upscaling. As shown in Fig. 6**b**−**d**, the CuI/BBO-CRO$_{BPY}$+P27/SnO$_2$/Pt photoelectrode with an area of 100 cm^2 exhibits an excellent ΔJ with 82.0 μA cm^{-2} and favorable stability. To ascertain the authenticity of our findings and establish the universality of the methodology, a comprehensive investigation was conducted across a range of photoelectrode areas spanning from 1 to 100 cm^2 (Fig. S25). The average ΔJ recorded across these diverse photoelectrode areas consistently registered at 80.6 μA cm^{-2} (Table S5). The meticulous assessment not only emphasizes the reliability of our findings but also highlights the inherent applicability of the method across diverse scales.
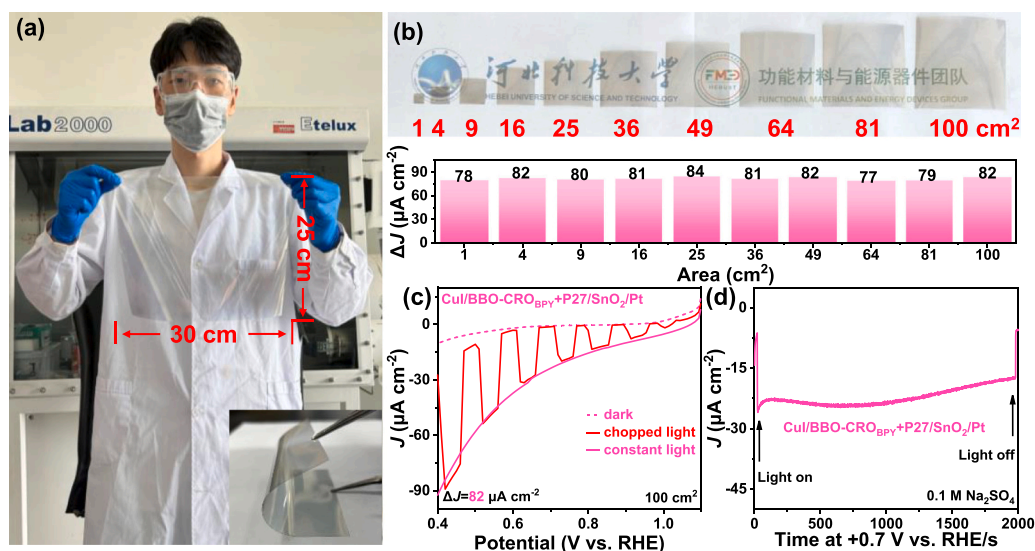
Fig. 6. The photographs of a CuI/BBO-CRO$_{BPY}$+P27/SnO$_2$/Pt photoelectrode with an area of (a) 750 cm^2 and (b) 100 cm^2. The image in (a) depicts a bendability test insert. (c) LSV cures of CuI/BBO-CRO$_{BPY}$+P27/SnO$_2$/Pt photoelectrode with an area of 100 cm^2 under constant and chopped light. (d) CA curves of CuI/BBO-CRO$_{BPY}$+P27/SnO$_2$/Pt photoelectrode with an area of 100 cm^2. (e) The ΔJ of different photoelectrode areas.

The consistent photocurrent response further enhances the robustness of our approach, thereby substantiating its potential for widespread implementation in the PEC reaction. The large-area photoelectrode, fabricated *via* the blade coating technique, maintained its exceptional photo-electrocatalytic activity, by exhibiting high light absorption efficiency and stable electron transfer rates. This seamless transition from a small-scale to a large-scale photoelectrode fabrication method provides robust support for the sustainable advancement of photoelectrochemical water-splitting technology. Our research not only represents a significant breakthrough in materials synthesis and processing methods but also paves the way for the utilization of flexible devices in green energy production, showcasing their potential in scientific research and practical applications.

4. Conclusions

We have successfully synthesized solution-processed BBO-CROs using intricately designed benzoxazole photosensitive molecules, employing micelles as nanoreactors for the reaction. The as-obtained BBO-CROs colloids were identified as electronic ink to fabricate panel-type photoelectrodes with a smooth and homogeneous surface in PEC water reduction. The UV–vis DRS spectra of BBO-CROs demonstrate their ability to efficiently absorb photons across the ultraviolet and infrared regions, while the prolonged PL fluorescence lifetimes signify enhanced charge carrier recombination suppression. The promising prospects of employing COF solution in PEC water reduction were successfully illustrated through the creation of HTL/BBO-CROs active layer/ELC/Pt full-devices utilizing readily processable BBO-CROs and the spinning coating technique. The optimized photoelectrodes with the architecture of CuI/BBO-CRO$_{PDA}$+P27/SnO$_2$/Pt, CuI/BBO-CRO$_{DHTA}$+P27/SnO$_2$/Pt, and CuI/BBO-CRO$_{BPY}$+P27/SnO$_2$/Pt result in ΔJ of 47.5, 72.3, and 86.5 μA cm^{-2} at 0.4 V *vs.* RHE, which is 118.8, 60.3 and 86.5 times higher than that of BBO-COF$_{PDA}$, BBO-COF$_{DHTA}$, and BBO-COF$_{BPY}$. In order to achieve large-scale preparation, we successfully employed the blade coating technology to prepare flexible large-area panel electrodes on ITO substrates using BBO-CRO$_{BPY}$ solution, yielding a 750 cm^2 photoelectrode with maintained flexibility, promising versatile applications for PEC water reduction. Among them, the photoelectrode with an area of 100 cm^2 consisting of CuI/BBO-CRO$_{BPY}$+P27/SnO$_2$/Pt demonstrates a remarkable ΔJ value of 82.0 μA cm^{-2} and exhibits favorable stability. This work not only addressed the bottleneck issue arising from

the limited processability of COFs but also paved the way for novel applications of large-scale flexible devices in green energy production.

CRediT authorship contribution statement

Haining Liu: Funding acquisition. **Pengda Zhai:** Investigation. **Ruijuan Zhang:** Investigation. **Xiaoming Li:** Methodology. **Yazhou Kang:** Methodology, Formal analysis, Data curation. **Shanlin Qiao:** Writing – review & editing, Supervision, Funding acquisition. **Ying Zhao:** Writing – review & editing, Supervision, Funding acquisition. **Boying Zhang:** Writing – original draft, Formal analysis. **Huimin Gao:** Methodology.

Declaration of Competing Interest

The authors declare that they have no known competing financial interests or personal relationships that could have appeared to influence the work reported in this paper.

Data availability

Data will be made available on request.

Appendix A. Supporting information

Supplementary data associated with this article can be found in the online version at doi:10.1016/j.apcatb.2024.123863.

References

[1] S.J. Davis, N.S. Lewis, M. Shaner, S. Aggarwal, D. Arent, I.L. Azevedo, S.M. Benson, T. Bradley, J. Brouwer, Y.-M. Chiang, C.T.M. Clack, A. Cohen, S. Doig, J. Edmonds, P. Fennell, C.B. Field, B. Hannegan, B.-M. Hodge, M.I. Hoffert, E. Ingersoll, P. Jaramillo, K.S. Lackner, K.J. Mach, M. Mastrandrea, J. Ogden, P.F. Peterson, D.

L. Sanchez, D. Sperling, J. Stagner, J.E. Trancik, C.-J. Yang, K. Caldeira, Net-zero emissions energy systems, Science 360 (2018) eaas9793.

[2] B. Zhang, L. Chen, Z. Zhang, Q. Li, P. Khangale, D. Hildebrandt, X. Liu, Q. Feng, S. Qiao, Modulating the band structure of metal coordinated salen COFs and an in situ constructed charge transfer heterostructure for electrocatalysis hydrogen evolution, Adv. Sci. 9 (2022) 2105912.

[3] J. Wang, Z. Zhang, S. Qi, Y. Fan, Y. Yang, W. Li, M. Zhao, Photo-assisted high performance single atom electrocatalysis of the N_2 reduction reaction by a Mo-embedded covalent organic framework, J. Mater. Chem. A 9 (2021) 19949–19957.

[4] H. Bai, F. Wang, Q. Ding, W. Xie, H. Li, G. Zheng, W. Fan, Construction of Frustrated Lewis Pair Sites in CeO_2–$C/BiVO_4$ for photoelectrochemical nitrate reduction, Inorg. Chem. 62 (2023) 2394–2403.

[5] F. Wang, Q. Ding, J. Ding, Y. Bai, H. Bai, W. Fan, Frustrated lewis pairs boosting photoelectrochemical nitrate reduction over $ZnIn_2S_4/BiVO_4$ heterostructure, Chem. Eng. J. 450 (2022) 138260.

[6] X. Li, W. Fan, Y. Bai, Y. Liu, F. Wang, H. Bai, W. Shi, Photoelectrochemical reduction of nitrate to ammonia over $CuPc/CeO_2$ heterostructure: understanding the synergistic effect between oxygen vacancies and Ce sites, Chem. Eng. J. 433 (2022) 133225.

[7] T. Li, M. Ruan, Z. Guo, C. Wang, Z. Liu, Modulation of Lewis and Brønsted acidic sites to enhance the redox ability of Nb_2O_5 photoanodes for efficient photoelectrochemical performance, ACS Appl. Mater. Interfaces 15 (2023) 11914–11926.

[8] Y. Wu, M. Ruan, Z. Guo, C. Wang, Z. Liu, Optimization of the IO_3 polar group of $BiOIO_3$ by bulk phase doping amplifies pyroelectric polarization to enhance carrier separation and improve the pyro-photo-electric catalytic performance, Appl. Catal. B 339 (2023) 123169.

[9] T. Li, Y. Zou, Z. Liu, Magnetic-thermal external field activate the pyro-magnetic effect of pyroelectric crystal ($NaNbO_3$) to build a promising multi-field coupling-assisted photoelectrochemical water splitting system, Appl. Catal. B 328 (2023) 122486.

[10] Q. Zhao, Z. Liu, Z. Guo, M. Ruan, W. Yan, The collaborative mechanism of surface S-vacancies and piezoelectric polarization for boosting CdS photoelectrochemical performance, Chem. Eng. J. 433 (2022) 133226.

[11] L. Yao, A. Rahmanudin, N. Guijarro, K. Sivula, Organic semiconductor based devices for solar water splitting, Adv. Energy Mater. 8 (2018) 1802585.

[12] K. Sivula, R. van de Krol, Semiconducting materials for photoelectrochemical energy conversion, Nat. Rev. Mater. 1 (2016) 15010.

[13] D. Zhang, H.-H. Cho, J.-H. Yum, M. Mensi, K. Sivula, An organic semiconductor photoelectrochemical tandem cell for solar water splitting, Adv. Energy Mater. 12 (2022) 2202363.

[14] Z. Zhao, S. Zhan, L. Feng, C. Liu, M.S.G. Ahlquist, X. Wu, K. Fan, F. Li, L. Sun, Molecular engineering of photocathodes based on polythiophene organic semiconductors for photoelectrochemical hydrogen generation, ACS Appl. Mater. Interfaces 13 (2021) 40602–40611.

[15] X. Li, X. Duan, Z. Liang, L. Yan, Y. Yang, J. Qiao, X. Hao, C. Zhang, J. Zhang, Y. Li, F. Huang, Y. Sun, Benzo[1,2-b:4,5-b']difuran based polymer donor for high-efficiency (>16 %) and stable organic solar cells, Adv. Energy Mater. 12 (2022) 2103684.

[16] H. Bronstein, C.B. Nielsen, B.C. Schroeder, I. McCulloch, The role of chemical design in the performance of organic semiconductors, Nat. Rev. Chem. 4 (2020) 66–77.

[17] S. Jin, O. Allam, S.S. Jang, S.W. Lee, Covalent organic frameworks: design and applications in electrochemical energy storage devices, Infomat 4 (2022) e12277.

[18] S. Qiao, M. Di, J.-X. Jiang, B.-H. Han, Conjugated porous polymers for photocatalysis: the road from catalytic mechanism, molecular structure to advanced applications, EnergyChem 4 (2022) 100094.

[19] T. He, Y. Zhao, Covalent organic frameworks for energy conversion in photocatalysis, Angew. Chem. Int. Ed. 62 (2023) e202303086.

[20] C. Dai, T. He, L. Zhong, X. Liu, W. Zhen, C. Xue, S. Li, D. Jiang, B. Liu, 2,4,6-triphenyl-1,3,5-triazine based covalent organic frameworks for photoelectrochemical H_2 evolution, Adv. Mater. Interfaces 8 (2021) 2002191.

[21] S. Xu, H. Sun, M. Addicoat, B.P. Biswal, F. He, S. Park, S. Paasch, T. Zhang, W. Sheng, E. Brunner, W. Hou, M. Richter, X. Feng, Thiophene-Bridged donor–acceptor sp^2-carbon-linked 2D conjugated polymers as photocathodes for water reduction, Adv. Mater. 33 (2021) 2006274.

[22] T. Sick, A.G. Hufnagel, J. Kampmann, I. Kondofersky, M. Calik, J.M. Rotter, A. Evans, M. Döblinger, S. Herbert, K. Peters, D. Böhm, P. Knochel, D.D. Medina, D. Fattakhova-Rohlfing, T. Bein, Oriented Films of Conjugated 2D covalent organic frameworks as photocathodes for water splitting, J. Am. Chem. Soc. 140 (2018) 2085–2092.

[23] J.M. Rotter, S. Weinberger, J. Kampmann, T. Sick, M. Shalom, T. Bein, D. D. Medina, Covalent organic framework films through electrophoretic deposition—creating efficient morphologies for catalysis, Chem. Mater. 31 (2019) 10008–10016.

[24] L. Yao, A. Rodríguez-Camargo, M. Xia, D. Mücke, R. Guntermann, Y. Liu, L. Grunenberg, A. Jiménez-Solano, V. Duppel, K. Sivula, T. Bein, H. Qi, U. Kaiser, M. Grätzel, B.V. Lotsch, Covalent organic framework nanoplates enable solution-processed crystalline nanofilms for photoelectrochemical hydrogen evolution, J. Am. Chem. Soc. 144 (2022) 10291–10300.

[25] S. Pradhan, F. Di Stasio, Y. Bi, S. Gupta, S. Christodoulou, A. Stavrinadis, G. Konstantatos, High-efficiency colloidal quantum dot infrared light-emitting diodes via engineering at the supra-nanocrystalline level, Nat. Nanotechnol. 14 (2019) 72–79.

[26] P.-F. Wei, M.-Z. Qi, Z.-P. Wang, S.-Y. Ding, W. Yu, Q. Liu, L.-K. Wang, H.-Z. Wang, W.-K. An, W. Wang, Benzoxazole-LInked Ultrastable Covalent Organic Frameworks for Photocatalysis, J. Am. Chem. Soc. 140 (2018) 4623–4631.

[27] H. Liu, H. Yan, W. Chen, Z. Xie, S. Li, W. Chen, T. Zhang, G. Xing, L. Chen, Donor-acceptor 2D covalent organic frameworks for efficient heterogeneous photocatalytic α-oxyamination, Sci. China Chem. 64 (2021) 827–833.

[28] X. Yan, H. Liu, Y. Li, W. Chen, T. Zhang, Z. Zhao, G. Xing, L. Chen, Ultrastable covalent organic frameworks via self-polycondensation of an A_2B_2 monomer for heterogeneous photocatalysis, Macromolecules 52 (2019) 7977–7983.

[29] H.H. Choi, J.Y. Baek, E. Song, B. Kang, K. Cho, S.-K. Kwon, Y.-H. Kim, A. Pseudo-Regular, alternating conjugated copolymer using an asymmetric monomer: a high-mobility organic transistor in nonchlorinated solvents, Adv. Mater. 27 (2015) 3626–3631.

[30] Y. Ji, C. Xiao, Q. Wang, J. Zhang, C. Li, Y. Wu, Z. Wei, X. Zhan, W. Hu, Z. Wang, R. A.J. Janssen, W. Li, Asymmetric diketopyrrolopyrrole conjugated polymers for field-effect transistors and polymer solar cells processed from a nonchlorinated solvent, Adv. Mater. 28 (2016) 943–950.

[31] R. Li, J. Byun, W. Huang, C. Ayed, L. Wang, K.A.I. Zhang, Poly(benzothiadiazoles) and their derivatives as heterogeneous photocatalysts for visible-light-driven chemical transformations, ACS Catal. 8 (2018) 4735–4750.

[32] B. Zhang, H. Liu, P. Zhai, R. Zhang, W. Wang, P. Khangale, D. Hildebrandt, X. Liu, S. Qiao, Well-defined conjugated reticular oligomer "blood cells" and conducting polymer "neurons" constructing "muscle"-biomimetic electrocatalysts for water electrolysis, Adv. Funct. Mater. 33 (2023) 2211440.

[33] W. Wang, Z. Yang, Y. Zhang, A. Wang, Y. Zhang, L. Chen, Q. Li, S. Qiao, Highly stable lithium metal anode enabled by lithiophilic and spatial-confined spherical-covalent organic framework, Energy Stor. Mater. 46 (2022) 374–383.

[34] H. Zhao, Z.-Y. Yuan, Progress and perspectives for solar-driven water electrolysis to produce green hydrogen, Adv. Energy Mater. 13 (2023) 2300254.

[35] W. Huang, Y. Hu, Z. Qin, Y. Ji, X. Zhao, Y. Wu, Q. He, Y. Li, C. Zhang, J. Lu, Y. Li, Highly crystalline and water-wettable benzobisthiazole-based covalent organic frameworks for enhanced photocatalytic hydrogen production, Natl. Sci. Rev. 10 (2022) nwac171.

[36] R. Shen, C. Qin, L. Hao, X. Li, P. Zhang, X. Li, Realizing photocatalytic overall water splitting by modulating the thickness-induced reaction energy barrier of fluorenone-based covalent organic frameworks, Adv. Mater. 35 (2023) 2305397.

[37] S. Yang, H. Lv, H. Zhong, D. Yuan, X. Wang, R.J.A.C. Wang, Transformation of covalent organic frameworks from N-acylhydrazone to oxadiazole linkages for smooth electron transfer in photocatalysis, Angew. Chem. Int. Ed. 134 (2022) e202115655.

[38] T. Zhou, L. Wang, X. Huang, J. Unruangsri, H. Zhang, R. Wang, Q. Song, Q. Yang, W. Li, C. Wang, K. Takahashi, H. Xu, J. Guo, PEG-stabilized coaxial stacking of two-dimensional covalent organic frameworks for enhanced photocatalytic hydrogen evolution, Nat. Commun. 12 (2021) 3934.

[39] Y. Yang, X. Chu, H.-Y. Zhang, R. Zhang, Y.-H. Liu, F.-M. Zhang, M. Lu, Z.-D. Yang, Y.-Q. Lan, Engineering β-ketoamine covalent organic frameworks for photocatalytic overall water splitting, Nat. Commun. 14 (2023) 593.

[40] R. Shen, X. Li, C. Qin, P. Zhang, X. Li, Efficient photocatalytic hydrogen evolution by modulating excitonic effects in Ni-intercalated covalent organic frameworks, Adv. Energy Mater. 13 (2023) 2203695.

[41] J. Ming, A. Liu, J. Zhao, P. Zhang, H. Huang, H. Lin, Z. Xu, X. Zhang, X. Wang, J. Hofkens, M.B.J. Roeffaers, J. Long, Hot π-electron tunneling of metal–insulator–COF nanostructures for efficient hydrogen production, Angew. Chem. Int. Ed. 58 (2019) 18290–18294.

[42] L. Wang, L. Zhang, B. Lin, Y. Zheng, J. Chen, Y. Zheng, B. Gao, J. Long, Y. Chen, Activation of carbonyl oxygen sites in β-ketoenamine-linked covalent organic frameworks via cyano conjugation for efficient photocatalytic hydrogen evolution, Small 17 (2021) 2101017.

[43] W.-K. Han, Y. Liu, X. Yan, Y. Jiang, J. Zhang, Z.-G. Gu, Integrating light-harvesting ruthenium(II)-based units into three-dimensional metal covalent organic frameworks for photocatalytic hydrogen evolution, Angew. Chem. Int. Ed. 61 (2022) e202208791.

[44] J. Hong, J. Kim, I. Hwang, Aging-induced Light-soaking effects and open-circuit voltage hysteretic behavior of inverted perovskite solar cells incorporating a hole transport metal halide layer via morphology-dependent inflow of iodide ions, J. Mater. Chem. C 7 (2019) 1173–1181.

[45] L. Yao, Y. Liu, H.-H. Cho, M. Xia, A. Sekar, B. Primera Darwich, R.A. Wells, J.-H. Yum, D. Ren, M. Grätzel, N. Guijarro, K. Sivula, A hybrid bulk-heterojunction photoanode for direct solar-to-chemical conversion, Energy Environ. Sci. 14 (2021) 3141–3151.

[46] H.-H. Cho, L. Yao, J.-H. Yum, Y. Liu, F. Boudoire, R.A. Wells, N. Guijarro, A. Sekar, K. Sivula, A semiconducting polymer bulk heterojunction photoanode for solar water oxidation, Nat. Catal. 4 (2021) 431–438.

[47] T.H. Lee, S.A.J. Hillman, S. Gonzalez-Carrero, A. Difilippo, J.R. Durrant, Long-lived charges in Y6:PM6 bulk-heterojunction photoanodes with a polymer overlayer improve photoelectrocatalytic performance, Adv. Energy Mater. 13 (2023) 2300400.

[48] A.R. Puente Santiago, M.F. Sanad, A. Moreno-Vicente, M.A. Ahsan, M.R. Cerón, Y.-R. Yao, S.T. Sreenivasan, A. Rodriguez-Fortea, J.M. Poblet, L. Echegoyen, A. New, Class of molecular electrocatalysts for hydrogen evolution: catalytic activity of $M_3N@C2n$ (2n = 68, 78, and 80) fullerenes, J. Am. Chem. Soc. 143 (2021) 6037–6042.

[49] J. Azevedo, S.D. Tilley, M. Schreier, M. Stefik, C. Sousa, J.P. Araújo, A. Mendes, M. Grätzel, M.T. Mayer, Tin oxide as stable protective layer for composite cuprous oxide water-splitting photocathodes, Nano Energy 24 (2016) 10–16.

[50] Q. Jiang, L. Zhang, H. Wang, X. Yang, J. Meng, H. Liu, Z. Yin, J. Wu, X. Zhang, J. You, Enhanced electron extraction using SnO_2 for high-efficiency Planar-structure $HC(NH_2)_2PbI_3$-based perovskite solar cells, Nat. Energy 2 (2016) 16177.

[51] S. Ni, H. Qu, Z. Xu, X. Zhu, H. Xing, L. Wang, J. Yu, H. Liu, C. Chen, L. Yang, Interfacial engineering of the $NiSe_2$/$FeSe_2$ π-π heterojunction for promoting oxygen evolution reaction and electrocatalytic urea oxidation, Appl. Catal. B 299 (2021) 120638.

[52] S. Qiao, B. Zhang, Q. Li, Z. Li, W. Wang, J. Zhao, X. Zhang, Y. Hu, Pore Surface engineering of covalent triazine frameworks@MoS_2 electrocatalyst for the hydrogen evolution reaction, ChemSusChem 12 (2019) 5032.

[53] T. Sick, A.G. Hufnagel, J. Kampmann, I. Kondofersky, M. Calik, J.M. Rotter, A. Evans, M. Döblinger, S. Herbert, K. Peters, D. Böhm, P. Knochel, D.D. Medina, D. Fattakhova-Rohlfing, T. Bein, Oriented films of conjugated 2D covalent organic frameworks as photocathodes for water splitting, J. Am. Chem. Soc. 140 (2018) 2085–2092.

[54] B. Zhang, H. Gao, Y. Kang, X. Li, Q. Li, P. Zhai, D. Hildebrandt, X. Liu, Y. Wang, S. Qiao, Molecular and heterojunction device engineering of solution-processed conjugated reticular oligomers: enhanced photoelectrochemical hydrogen evolution through high-effective exciton separation, Adv. Sci. (2024) 2308535, https://doi.org/10.1002/advs.202308535.

[55] Z. Liu, X. Wang, T. Lu, A. Yuan, X. Yan, Potential optical molecular switch: lithium@cyclo[18]Carbon complex transforming between two stable configurations, Carbon 187 (2022) 78–85.

[56] T. Lu, F. Chen, Multiwfn: a multifunctional wavefunction analyzer, J. Comput. Chem. 33 (2012) 580–592.

[57] Y. Qian, Y. Han, X. Zhang, G. Yang, G. Zhang, H.-L. Jiang, Computation-based regulation of excitonic effects in donor-acceptor covalent organic frameworks for enhanced photocatalysis, Nat. Commun. 14 (2023) 3083.

[58] J. Yuan, J. Yuan, X. Tian, Y. Liu, J. Sun, Insights into the photobehavior of fluorescent oxazinone, quinazoline, and difluoroboron derivatives: molecular design based on the structure–property relationships, J. Phys. Chem. C. 121 (2017) 10626–10627.

[59] Z. Mi, T. Zhou, W. Weng, J. Unruangsri, K. Hu, W. Yang, C. Wang, K.A.I. Zhang, J. Guo, Covalent organic frameworks enabling site isolation of viologen-derived electron-transfer mediators for stable photocatalytic hydrogen evolution, Angew. Chem. Int. Ed. 60 (2021) 9642–9649.

[60] J.-L. Bredas, Mind the gap!, Mater. Horiz. 1 (2014) 17–19.